

Passive vibration compensation in scanning white-light interferometry

STANISLAV TERESCHENKO,^{1,*} PETER LEHMANN,¹ LISA ZELLMER,² AND ANGELIKA BRUECKNER-FOIT²

¹Measurement Technology, Department of Electrical Engineering and Computer Science, University of Kassel, Wilhelmshoeher Allee 71, 34121 Kassel, Germany

²Institute for Materials Engineering, University of Kassel, Moenchebergstrasse 3, 34109 Kassel, Germany

*Corresponding author: s.tereschenko@uni-kassel.de

Received 31 May 2016; revised 11 July 2016; accepted 11 July 2016; posted 12 July 2016 (Doc. ID 267390); published 2 August 2016

We present a passive vibration compensation approach in scanning white-light interferometry (SWLI). A point-wise distance measuring interferometer (DMI) obtains fast temporal distance changes during the white-light depth-scan of an aerial-measuring Michelson white-light interferometer for topography measurement. Both interferometers share a part of the optical path so that the measurement spot of the DMI is within the field of view of SWLI. With the real positions of the interferometer with respect to the measuring object during the depth scan known from DMI measurements, we can compensate for the influence of unintentional distance changes caused by environmental vibrations or scanner nonlinearities. By reordering of the captured image frames and improved correlogram interpolation, we are able to reconstruct correct signals from completely distorted (and unusable) SWLI signals. Although the basic idea of the system already has been published, we improved the signal reconstruction technique so that the specimen's topography measurement can be obtained with the same accuracy as without any vibrations or scan distortions influence. In addition, we demonstrate the feasibility of the approach by different practical measurements with and without vibrations. © 2016 Optical Society of America

OCIS codes: (120.2830) Height measurements; (120.5050) Phase measurement; (120.5060) Phase modulation; (180.3170) Interference microscopy; (120.7280) Vibration analysis; (150.3045) Industrial optical metrology.

<http://dx.doi.org/10.1364/AO.55.006172>

1. INTRODUCTION

Scanning white-light interferometers are well-established optical instruments for 3D measurement of micro- and nanostructures with high accuracy [1,2]. The measuring procedure is based on a so-called depth scan, whereby the distance between the interferometer and the specimen varies continuously. During this scanning process, a camera captures several hundred images at equidistant axial positions. By evaluation of the interference contrast and phase of the signal from each camera pixel along the scanning direction, the 3D topography is obtained [3–5].

Scanning white-light interferometry (SWLI) is well-suited for the measurement of structured surfaces such as step height structures [e.g., of microelectromechanical-systems (MEMS)] but also for the surface inspection in the automotive industry (e.g., shape and roughness inspection of valve seats in common rail diesel injection systems) [6]. The common trend in the industry is 100% quality control, which demands the integration of measurement systems into the production process. On the other hand, the high accuracy of SWLI measurement in the nanometer range can only be achieved in vibration-reduced environments (e.g., in a lab on a vibration-isolated optical table). Due to mechanical vibrations, the use of white-light

interferometers on the shop-floor level is difficult and requires a lot of compensation effort.

Over the last few decades, different vibration compensation techniques have been presented. They can be divided into active and passive approaches. Active vibration compensation aims to measure the vibration and to compensate the optical path length in the reference or measurement arm of the interferometer by moving the reference plane [7–9], the specimen, or the whole interferometer [10] during the measurement. Some approaches vary the relative phase in the reference arm by means of acousto-optic [11] or electro-optic [12] modulators. In the case of passive vibration compensation, the disturbance is captured during the topography measurement. The compensation itself usually takes place following the measurement by applying different algorithms to the measured data. The algorithms pursue different approaches. By evaluation of signals in the frequency domain, height information can be extracted from distorted signals [13,14]. Combination of fast distance measurements with area-measuring interferometers allows either correcting the errors introduced by the scanner [15–17] or even using the vibrations for phase shifting and applying a custom random-phase-shift algorithm [18] to be able to obtain surface topographies with high accuracy.

So-called single-shot techniques deserve special mention. With polarizing optics three- or four-phase shifted interferograms are generated and simultaneously captured either by three or four detectors (cameras) [19]. With a so-called *pixelated camera mask*, phase-shifted interference signals are captured by a single camera chip [20,21]. Digital holographic microscopy (DHM) is another single-shot technique that allows accurate vibration-insensitive measurements [22,23].

This paper describes a passive vibration compensation technique similar to an approach introduced by Olszak and co-workers [15,16] in order to reduce the effect of nonlinearities of the depth scanner on the height measurement. The idea is based on simultaneous measurement of white-light interference patterns (camera images) and the corresponding positions of the depth scanner during the scan. In our system, vibration compensation takes place after the measurement by reordering samples according to their real consecutive depth axial position, followed by an interpolation on an equidistant sampling interval. After the correction of the correlograms, the surface topography can be obtained with common fringe contrast and phase evaluation algorithms [3–5].

In Section 2 we introduce the sensor setup and describe the measuring procedure. In the next section, we present the signal evaluation algorithms and especially the correction of the SWLI signals. In Section 4, we show measurement results of typical objects such as spheres, roughness, and groove-depth standards. Section 5 offers conclusions and shows an outlook to future work.

2. SENSOR CONFIGURATION

The sensor is a Michelson interferometer, which combines a white-light source (white LED) for areal topography measurements and an infrared laser source with a focused spot for point-wise distance measurements. The microscope objective lens (MO) and the Michelson interference arrangement are common parts of both systems. Thus, the laser spot is inside the field of view of the interference microscope. Figure 1 shows a scheme of the sensor setup, and Fig. 2 shows the photograph of the whole interferometer.

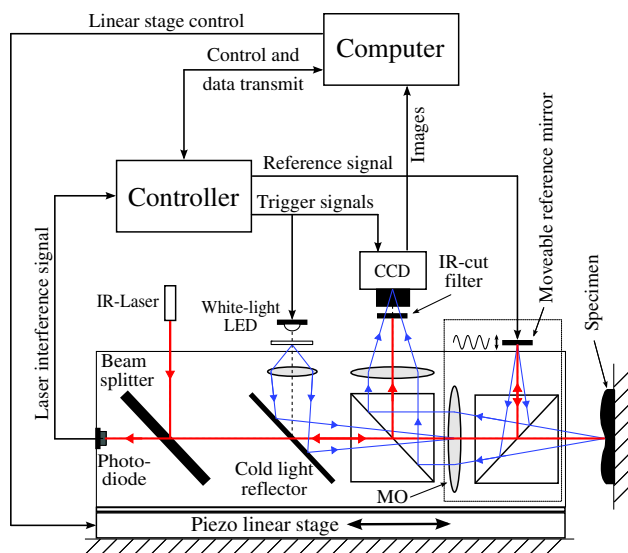


Fig. 1. Schematic of the sensor setup with signals and dataflow.

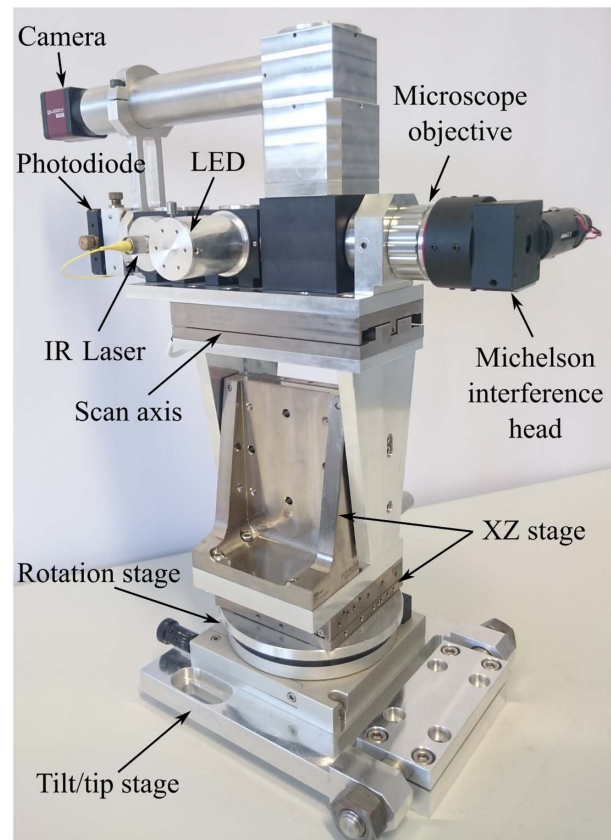


Fig. 2. Photograph of the sensor with additional XZ, rotation and tilt/tip stages used to adjust the sensor with respect to the specimen.

Additional components of this setup in comparison with a usual scanning white-light interferometer are optical filters and the movable reference mirror. Optical filters separate white-light and laser wavelength regimes from each other; in particular, the camera captures only white-light interferences due to the infrared cut filter in front of the CCD sensor. The cold-light reflector blocks the white-light. Thus, the photodiode captures only infrared laser interference intensities. We utilize the moveable reference mirror to generate a periodical optical path length modulation (OPLM) in the reference arm of the interferometer [24–26]. The mirror is a small piece of silicon wafer mounted on an inductive buzzer that oscillates with few kilohertz and an amplitude of approximately 1 μm . The periodic OPLM is necessary to generate a phase-modulated laser interference signal. The phase evaluation of this signal allows reliable and robust length measurement during the depth scan. For distance measurements, heterodyne interferometers are usually used. However, acousto-optical modulators and polarization optics are needed to perform fast and high-accuracy measurements. These additional components increase the cost of the system and make it less suitable for polarization-dependent surfaces and structures. Our system uses an unpolarized laser diode, which mainly contributes to additional costs in comparison to common white-light interferometers without any additional distance measuring system.

Because DMI and SWLI use the same reference mirror, they need to be synchronized with each other in order to reduce the

blurring of white-light interference signals by periodic mirror movement. At the turning points of the reference mirror, the momentary movement speed is zero. Hence, by triggering the camera and the LED only at these positions, we can nearly completely avoid the blurring of camera images. Usually, SWLI measurements are highly dependent on the ratio of the camera sampling rate and vibrational frequency [27]. However, by driving the LED with short pulses of approximately 7.5–10 μs , we can additionally reduce the influence of environmental vibrations on camera images during the exposure time, virtually freezing the movement. By use of such short light pulses even in the presence of high mechanical vibrations (e.g., 100 Hz with peak-to-valley values of 150 nm = $\lambda_{\text{center}}/4$), the distance change during the illumination time is below 0.5 nm. Even if the full dynamic range of the CCD chip is used, it will result in an intensity change lower than two digits on an 8-bit camera image.

The sensor was designed for measurements in a fatigue-testing machine [28]. For this purpose, the depth scan is performed by a horizontal piezo-driven linear stage (see Fig. 1), which moves the whole interferometer toward the specimen.

3. SIGNAL EVALUATION

During the depth scan, only raw interference signals and trigger timestamps are recorded. The correction of white-light correlograms is carried out subsequent to the measurement.

A. Laser Interference Signal

To determine the real positions of the images, it is at first necessary to evaluate the laser interference signal and to obtain the distance course of the interferometer with respect to the specimen during the depth scan. A section of the interference signal with the corresponding electrical excitation signal is shown in Fig. 3.

The reference mirror motion is not exactly known at that point; it has the same frequency as the excitation signal, but is delayed due to mechanical damping and the inductive behavior of the buzzer. The amplitude of the mirror motion can be calculated from the frequency of the signal $I_{\text{AC}}(t)$ defined in Eq. (2) and is approximately 611 nm in the signal shown in Fig. 3.

Any optical path length change (reference mirror movement, linear depth scan, vibrations) is encoded in the phase of the interference signal. Several approaches to extract the phase information from the signal were published before

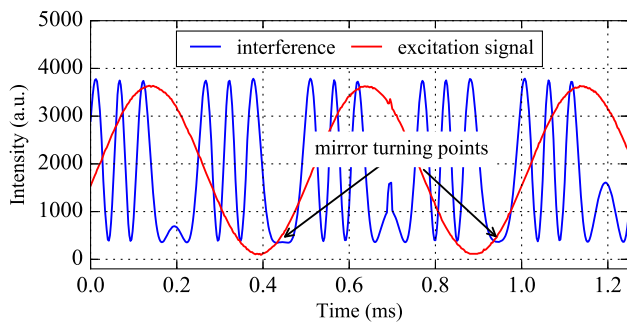


Fig. 3. Laser interference signal with the electric excitation signal; the interference signal is evaluated between two subsequent mirror turning points at falling and rising flanks of the mirror movement course.

[24–26,29–31]. The most interesting approaches are the single-point discrete Fourier transform (SP-DFT), also known as phase lock-in technique, and the Hilbert transform. The advantage of the Hilbert transform is a high position data rate, because for each sampling point, a phase value and thus, a position, is calculated. However, this technique has drawbacks at the turning positions of the reference mirror. The interference signal frequency goes toward zero, and the phase pointer changes its sign. Any noise in the signal at these positions can result in abrupt phase jumps and massively distorts the distance measurement. In comparison to the Hilbert transform, the SP-DFT is more robust, but has the disadvantage of producing a much lower position data rate, because only two position values per period of the mirror oscillation can be gained. Nonetheless, we use the SP-DFT approach because of its robustness and relatively simple implementation. The actual oscillation frequency of the reference mirror is 2 kHz, which results in a 4 kHz position data rate by evaluation of the interference signal at both flanks. As long as the maximal distance change between two consecutive position values is smaller than a quarter of the laser wavelength, a continuous distance course can be obtained.

The AC part of the laser interference signal is given by Eq. (1):

$$I_{\text{AC}}(t) = I_0 \cos \left(\frac{4\pi}{\lambda_0} [\hat{z}_0 \cos(2\pi f_0 t) + z(t)] \right), \quad (1)$$

where I_0 is the interference amplitude, λ_0 is the laser wavelength, \hat{z}_0 and f_0 are deflection amplitude and excitation frequency of the reference mirror, and $z(t)$ are arbitrary distance changes during the depth scan. From the signal evaluation perspective, it would be easier to perform a triangular movement of the reference mirror, because this leads to an interference signal (apart from the mirror turning points) with only a single frequency component and would allow the use of less computationally expensive algorithms like Hariharan *et al.* [30] or the integrating-bucket technique [31] for phase evaluation. In practice, however, triangular excitation signals lead to higher harmonics in the movement trajectory of the mirror, and therefore, more frequency components occur in the interference signal. Therefore, we use a sinusoidal excitation signal and evaluate the signal sections between the mirror turning points where the mirror trajectory is approximately linear. In this case the interference signal can be approximated by Eq. (2):

$$I_{\text{AC}}(t) \approx I_0 \cos \left(\frac{4\pi\hat{z}_0}{\lambda_0} 2\pi f_0 t + \varphi(t) \right), \quad (2)$$

with the fringe frequency $4\pi\hat{z}_0 f_0 / \lambda_0 = f_d$. Under the assumption that the mirror movement does not differ from period to period, the changes in the optical path length are encoded in the phase value $\varphi(t)$, which needs to be determined. As mentioned before, a single-point DFT is an appropriate and robust method to calculate the phase value:

$$\varphi_p = \arg \left(\sum_{n=0}^{N-1} I(n) W(n) \exp \left(-i2\pi n \frac{f_d}{f_s} \right) \right), \quad (3)$$

with the sampling frequency f_s , a window function $W(n)$, and the sampled interference signal $I(n)$. The window function is used to avoid the leakage. The $\arg()$ function calculates the

phase of a complex value in the range of $(-\pi, \pi]$. Assuming that the consecutive phase values φ_p do not change by more than $\pm\pi$, they can be unwrapped, and a continuous phase course φ_{unwr} results. The following equation:

$$z = \frac{\lambda_0}{4\pi} \varphi_{unwr} \quad (4)$$

converts phase to distance values z .

B. Uncertainty Analysis of DMI

Dominant disturbances that can generate an uncertainty in DMI phase measurement are: variation of excitation mirror amplitude and frequency, wavelength drift of the laser diode, harmonics in the excitation mirror signal, sampling jitter, additive random noise, and detector nonlinearity. We use a set of simulated data to show the impact of disturbances on the distance measurement result. The same nominal values as in the presented DMI are used: mirror excitation amplitude and frequency: $\hat{z}_0 = 611$ nm and $f_0 = 2$ kHz, respectively, sampling rate $f_s = 400$ kHz, laser wavelength $\lambda_0 = 850$ nm, and number of sample points per signal section $N = 100$.

Sinusoidal electrical excitation signal generation and interference signal sampling are performed by the same microcontroller unit (MCU). The clock signals are derived from a common single master clock. Any change in clock frequency equally changes in the sampling frequency of the analog-to-digital converter (ADC) and the excitation signal frequency of the digital-to-analog converter (DAC). Therefore, if a frequency change occurs, it has no impact on the phase evaluation result.

The amplitude of the reference mirror movement can vary depending on electrical characteristics of the amplifier or simply by varying of supply voltage. The distance measurement error by varying the excitation signal amplitude around the nominal amplitude in a range of ± 50 nm varies by ± 0.62 nm and results in a constant offset of the distance course. Before each measurement, the interference fringe frequency [see Eq. (2)] is determined by the Fourier-transform of the interference signal. Thus the change in mirror oscillation amplitude will be considered during signal evaluation.

The stability of the laser source is very important for distance measurements. A wavelength deviation $\Delta\lambda$ affects the distance measurement as a proportionality factor. The distance measurement error can be determined by the following equation:

$$\Delta z = \frac{\Delta\lambda l}{\lambda}, \quad (5)$$

where l describes the deviation from zero optical path length difference (OPD). In case of the presented DMI in combination with SWLI, the DMI always measures around the zero OPD. Under assumption of typical scan range for SWLI from 10 to 100 μm and a wavelength change $\Delta\lambda = 0.1$ nm of the distributed feedback (DFB) laser diode, the maximal distance error is 1.17 nm and 11.76 nm, respectively. For comparison, the linearity error of the linear piezo stage used for the depth scan is 5 nm over a range of 20 μm .

The dependence of distance measurement on different harmonics in the excitation signal and thus in phase shift is shown in Fig. 4. Odd harmonics generate lower error in phase measurement as they make the excitation signal shape more similar

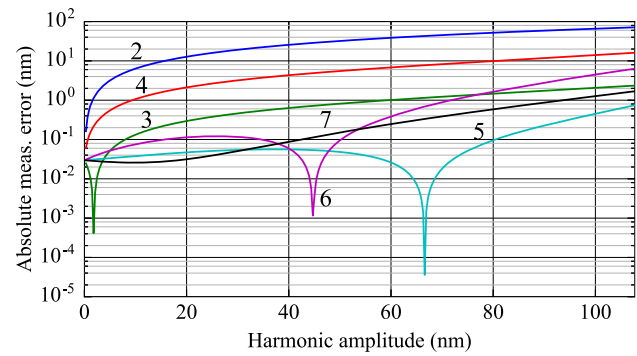


Fig. 4. Distance measurement error as function of different harmonic amplitudes.

to a triangle function, which leads to linear phase shift. Fourier analysis of the measured excitation signal revealed negligible small (below 1 %) harmonics in the signal (i.e., the amplitudes are below 1 nm).

The uncertainty due to additive random noise linearly increases with the noise level. The rms distance error is 0.13 nm at 1% and 1.3 nm at 10% noise amplitude, compared to signal amplitude for $N = 100$ sampling points per signal section. A similar linear behavior can be observed if sampling jitter occurs. The rms measurement error is 0.0086 nm at 1% and 0.086 nm at 10% random cycle-to-cycle jitter noise, which is more than one decade lower than the additive random noise contribution and can be neglected by using well-designed hardware with jitter errors around 200 ps.

Detector nonlinearity of order $n \geq 2$ can be expressed by the following equation [29]:

$$\Delta I = q\zeta \left[\left(\frac{I-q}{q} \right)^2 - \frac{1}{2} \right] \left(\frac{I-q}{q} \right)^{(n-2)}, \quad (6)$$

where ΔI is the deviation from linear fit to the measured signal I , and q is the mean intensity. ζ is the maximal deviation from linear over the full dynamic range of the detector. Simulations for $n = 2$, $n = 3$, and $n = 4$ show the rms distance errors of 0.054 nm, 0.078 nm, and 0.14 nm, respectively, over a full phase cycle for a 1% detector nonlinearity. These results are comparable with those presented in [29].

To check the uncertainty experimentally, repeatability measurements over a time range of 50 s were performed on a static object surface. Figure 5 shows the result. A standard deviation of 0.37 nm is achieved, which is in the same accuracy range as similar DMI systems [25,26].

C. Correction of White-Light Interference Signals

During the depth scan, an equidistant sampling period with an uncertainty in the range of few tens of nanometers is assumed. Deviations from the nominal sampling interval reduce the accuracy of the measurement. Depending on the evaluation strategy and the number of sampling points, some algorithms are more robust than others. However, even the best algorithms cannot handle errors that occur if the deviation in the sampling interval becomes too large. Because of the knowledge of the real z axis position of each camera image and thus the position of each sampling point in the image stack, we can rearrange the

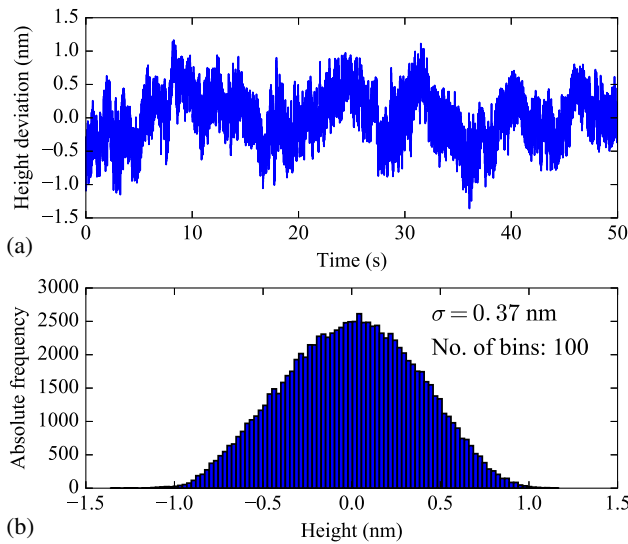


Fig. 5. Repeatability measurement on a static surface in (a) vibration-isolated environment and (b) the corresponding histogram.

correlograms in the desired order. The reordering process is explained in Fig. 6.

After reordering the interference signals, they are in the desired order, but the sampling interval is nonequidistant. Common signal processing algorithms require equidistant sampling points to calculate reliable height values. Therefore, we interpolate the reordered signals on an equidistant sampling interval in order to increase the accuracy of the evaluation.

Linear interpolation is the easiest and fastest way to do this. It requires only linear equations between consecutive reordered sampling points in order to calculate new intensity values at the desired positions. This calculation can be realized by Eq. (7):

$$I(u) = I_k + \frac{I_{k+1} - I_k}{z_{k+1} - z_k} (u - z_k), \quad (7)$$

where u is the desired position between two consecutive positions z_k, z_{k+1} , which belong to intensity values I_k, I_{k+1} .

In many cases, linear interpolation is good enough to reconstruct the signals, and the height values obtained from these signals are nearly the same as those obtained from signals measured under approximately ideal conditions without vibrations [28,32]. Nonetheless, under unfavorable conditions (e.g., longer gaps

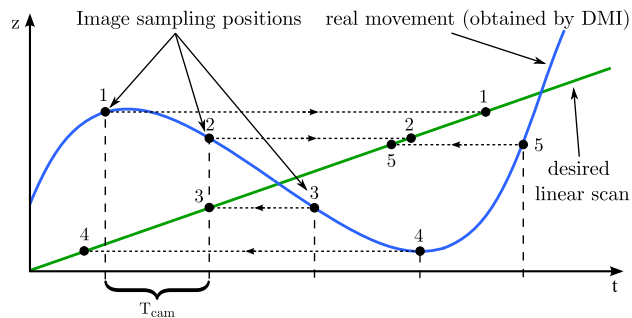


Fig. 6. Reordering procedure: equidistant temporal sampling results in a nonequidistant spatial sampling in presence of vibrations or scanner nonlinearities; after the image reordering, the spatial sampling interval is still nonequidistant.

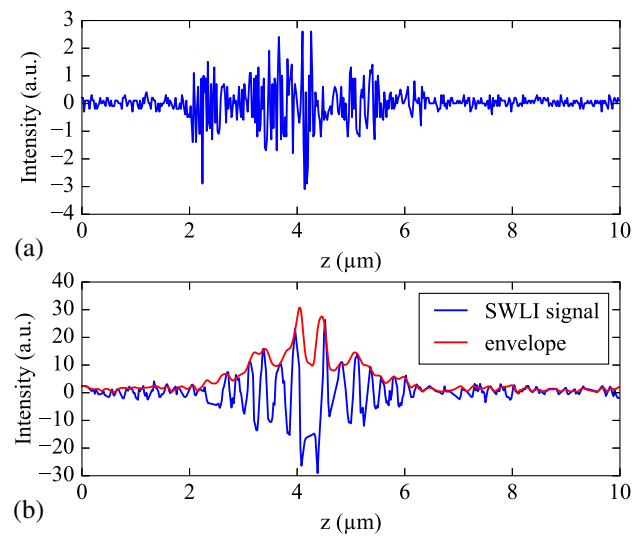


Fig. 7. (a) Measured signal with disturbances due to vibration; (b) reconstructed SWLI signal with missing sample points in the middle of the signal resulting from linear interpolation. The signal envelope shows two maxima with approximately the same intensity, leading to errors in height determination.

without intensity values) linear interpolation cannot generate reasonable interference signals. Figure 7 shows a SWLI signal with a larger gap around the maximum interference contrast.

To improve the correction of white-light interference signals, we use a so-called trigonometric approximation [33]. The underlying idea is to fit several trigonometric functions with different frequencies, amplitudes, and phases to the rearranged SWLI signals. A similar approach was introduced by Liesener *et al.* [34]. The Fourier transform of a white-light interference signal with a Gaussian envelope shape shows only a few frequency components that contribute to the signal in the spatial domain. The power spectral density outside of this frequency range is zero in the ideal case or contains undesirable noise in real measurements. Figure 8 shows a simulated SWLI

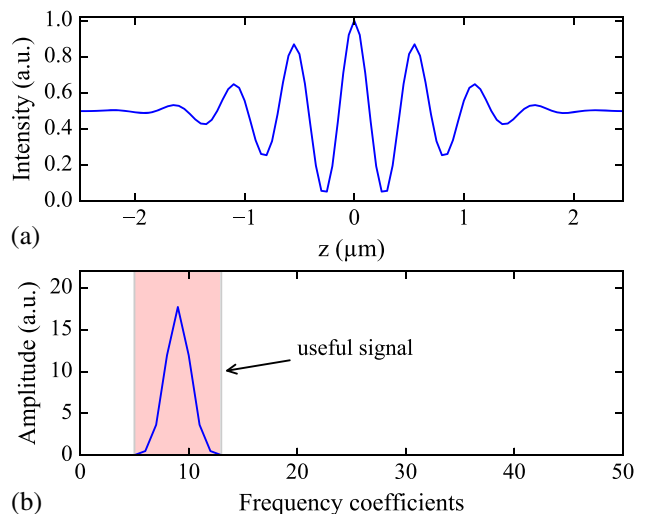


Fig. 8. (a) Simulated SWLI signal and (b) corresponding Fourier transform. Only a small range of frequency coefficients contribute to the signal.

signal with the corresponding Fourier transform and the range of frequency coefficients contributing to the signal. Usually, it is enough to fit ~ 15 to 30 sine and cosine function pairs (depending on the sampling interval, the number of sample points, and the spectrum of the light source) for the complete reconstruction of an interference signal. The SWLI signal can be approximated by the following equation:

$$f(z) = a_0 + \sum_{n=N_1}^{N_2} (a_n \cos(nz) + b_n \sin(nz)), \quad a_n, b_n \in \mathbb{R}. \quad (8)$$

Here, the position z is normalized to the range of $[0, 2\pi)$ and the index n is inside the mentioned interval of frequency coefficients. The least squares minimization problem is then defined as

$$\min \sum_{k=1}^M (I(z_k) - f(z_k))^2 = \min \|\mathbf{y} - \mathbf{f}\|^2 = \min \|\mathbf{y} - \mathbf{A}\mathbf{x}\|^2, \quad (9)$$

where $\mathbf{y} = (I(z_1) \cdots I(z_M))^T$ and $\mathbf{f} = \mathbf{A}\mathbf{x}$ with $\mathbf{x} = (a_0, a_{N_1}, b_{N_1}, \dots, a_{N_2}, b_{N_2})^T$ and

$$\mathbf{A} = \begin{pmatrix} 1 & \cos(N_1 z_1) & \sin(N_1 z_1) & \cdots & \cos(N_2 z_1) & \sin(N_2 z_1) \\ \vdots & \vdots & \vdots & \vdots & \vdots & \vdots \\ 1 & \cos(N_1 z_M) & \sin(N_1 z_M) & \cdots & \cos(N_2 z_M) & \sin(N_2 z_M) \end{pmatrix}. \quad (10)$$

The sought vector \mathbf{x} results from the solution of the following linear equation system:

$$\mathbf{A}^T \mathbf{A} \mathbf{x} = \mathbf{A}^T \mathbf{y}. \quad (11)$$

Care must be taken by simultaneously estimating several coefficients. The frequency range should be determined from a signal measured without vibrations and with equidistant sampling interval. By selecting too many frequency values in combination with nonequidistant sampling, there can be some correlations between different coefficients, and the matrix $\mathbf{A}^T \mathbf{A}$ can be ill-conditioned [35]; thus the approximation fails. However, as long as the linear equation system is overdetermined (matrix \mathbf{A} has fewer columns than rows), sample positions z are unique and monotonously increasing and selected sine and cosine functions are orthogonal to each other, the matrix $\mathbf{A}^T \mathbf{A}$ can be inverted, and the vector \mathbf{x} can be determined.

Finally, reconstructed SWLI signals are obtained by applying Eq. (8), using the results from Eq. (11) at the desired sampling positions.

In most cases, trigonometric approximation should be preferred compared to linear interpolation, because it effectively suppresses thermal camera and analog-to-digital (A/D) conversion noise and can handle longer gaps with missing points, due to periodic functions similar to the shape of the interference signal. In Fig. 9(a), the correlogram according to Fig. 7(b) is shown again. Applying the trigonometric approximation improves the result, as Fig. 9(b) demonstrates. The gap in the middle of the signal is effectively filled with data points. However, the drawback of this technique is much higher computational effort

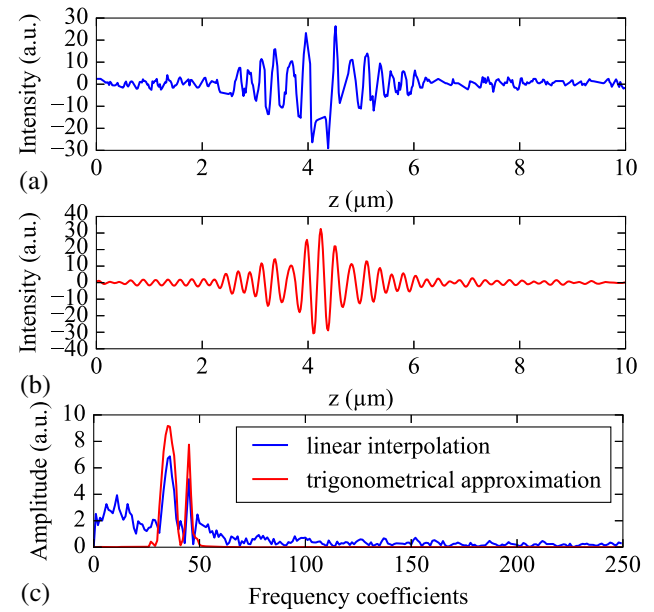


Fig. 9. Comparison between linear interpolation and trigonometric approximation: the same correlogram, which was used for linear interpolation [Fig. 7 or subfigure (a)] is trigonometrically approximated in (b). (c) shows the corresponding frequency spectra. The smaller peak in (c) results from the blue part of the spectrum of the cold white LED used for our measurements.

compared to linear interpolation. Trigonometric approximation requires $H \cdot (M_{P \times Z} \cdot M_{Z \times W} + M_{Z \times P} \cdot M_{P \times W})$ matrix multiplications, while linear interpolation requires only $2 \cdot Z \cdot H \cdot W$ multiplications and $Z \cdot H \cdot W$ additions, where Z is the number of captured images, P is the number of trigonometric polynomials, and W and H are dimensions of each image. In the next section, we show results obtained from linearly and trigonometrically reconstructed SWLI signals.

4. RESULTS

In previous publications [28,32], we demonstrated the performance of the vibration compensation method with artificial vibrations generated by a piezo-driven actuator at well-defined frequencies. The measuring object was a specular reflecting plane surface. In this paper, we present measurement results obtained under realistic conditions on different surfaces, such as steel specimens for fatigue-testing machine, sphere, roughness, and groove-depth standards.

As mentioned before, at first Fig. 10 shows topographies obtained from uncorrected, linearly interpolated and trigonometrically approximated SWLI signals. The topography in Fig. 10(a) is totally distorted. The measured height values jump around a few micrometers, although the measuring object is a diamond-milled plane mirror with maximum height differences below 100 nm. The second subfigure, 10(b), shows fewer height jumps than the first subfigure, but there are still areas with abrupt height changes resulting from phase jumps in the signal evaluation. Phase jumps result from erroneous fringe order estimation that is based on the preceding envelope evaluation. For example, the signal in Fig. 7(b) has a larger gap in the

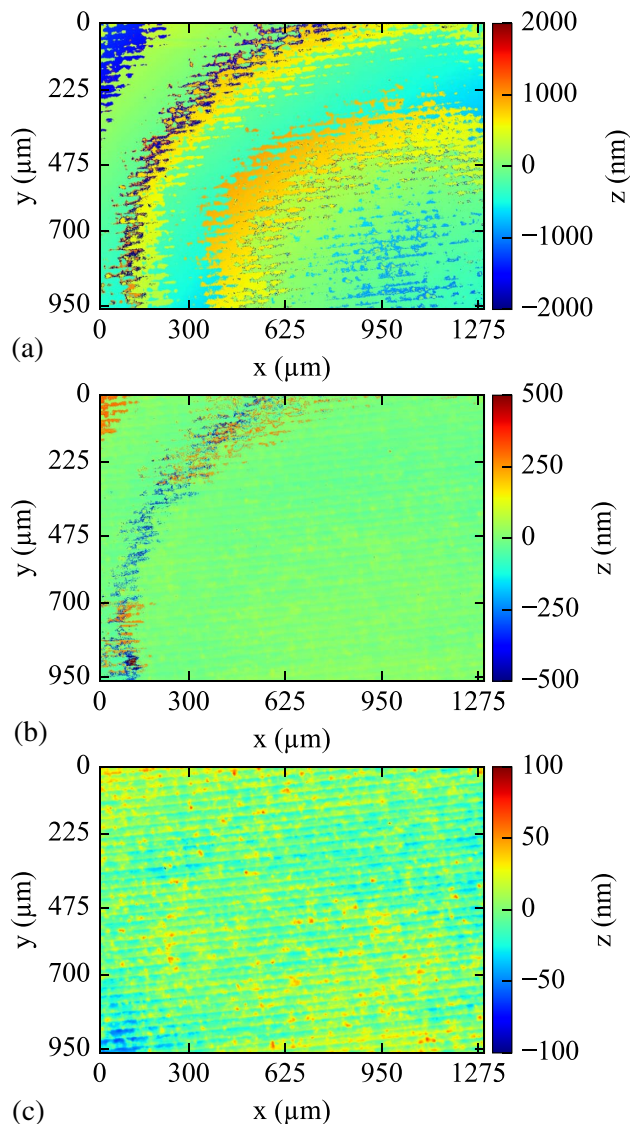


Fig. 10. Topographies obtained from differently reconstructed SWLI signals. (a) Uncorrected signals, (b) reordered and linearly interpolated signals, and (c) reordered and trigonometrically approximated signals.

middle of the correlogram. The signal envelope shows two local maxima with approximately the same height. It depends on the signal noise, which, of these two maxima, will be chosen for fringe order estimation. In the last subfigure, 10(c), the correct topography without any height jump is shown. The grooves in the topography result from the diamond-milling process. The standard deviation of the difference between these topography data and topography data obtained for the same field of view but without vibrations is only 2.19 nm.

As mentioned before, the sensor was designed for measurements in a fatigue-testing machine. The following result was obtained directly inside the machine and demonstrates the capability for vibration compensation. A polished steel specimen, prepared for cyclic loading tests, was used as a measurement object. The measurement was not carried out during the cyclic loading, because in that case the specimen moves laterally

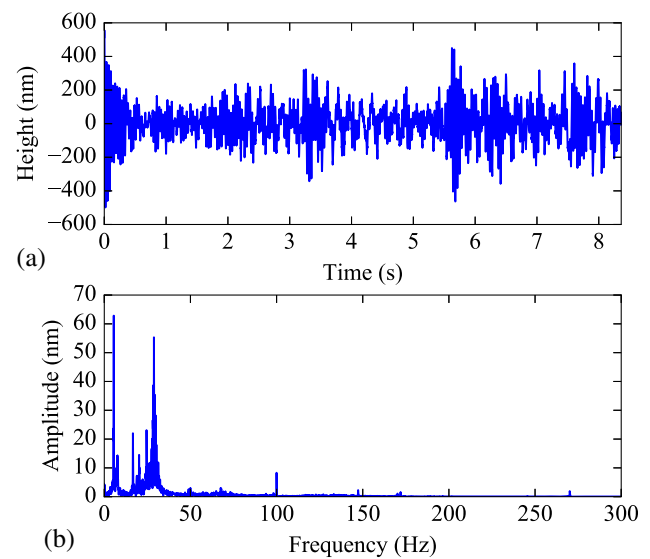


Fig. 11. (a) Distance deviation from linear ramp (10 μm) during a depth-scan and (b) corresponding frequency spectrum.

by several tens of micrometers, but with activated force control loop. In that case, the fatigue-testing machine pulls on the specimen with constant force. Several hydraulic pumps are active during this measurement, and there are a lot of vibrations in the environment. Figure 11(a) shows the distance deviations from the linear ramp during the depth scan, whereas Fig. 11(b) displays the corresponding frequency spectrum.

The vibrations occur primarily in the range between 0 and 30 Hz, but there is also a significant peak at 100 Hz that corresponds to AC motors of hydraulic pumps. The vibration compensation algorithm compensates for these vibrations, as can be seen in Fig. 12.

The data where the topography shown in Figs. 12(a) and 12(b) is based on was measured inside the fatigue-testing machine in the presence of the disturbances shown in Fig. 11. For comparison, Fig. 9(c) shows nearly the same surface section measured without vibrations in the lab on a vibration-damped optical table. It is not possible to compare the topographies according to Figs. 12(b) and 12(c) directly by subtraction because they are laterally misaligned. In addition, by clamping the specimen in the testing machine, it turns slightly and changes its topography. However, the difference between two topographies obtained in consecutive measurements inside the machine at the same lateral position results in a standard deviation of only 0.76 nm.

The following results were obtained in the lab on an optical table. However, mechanical vibrations were generated by a DC motor with an imbalanced axle mounted close to the interferometer on the same table. We used Halle roughness standards 4058/03A1 with nominal R_a and R_z values of 0.22 μm and 1.69 μm , respectively, and 4058/03A3 with $R_a = 1.65 \mu\text{m}$ and $R_z = 7.96 \mu\text{m}$. Rough surfaces are usually not a big challenge for white-light interferometers. As long as the modulation depth of SWLI signals is sufficient to detect the maximum coherence peak, an unambiguous height value can be determined. Surfaces illuminated by laser light tend to generate speckles and therefore decrease the modulation depth of an interference

signal. In the presented interferometer, a collimated infrared laser beam is focused by the microscope objective. The diameter of the laser spot on the surface is approximately $65\text{ }\mu\text{m}$, so that the interference signal represents an average over quite a big area. As expected, the modulation depth of the laser interference signal is much lower now, compared to a specularly reflecting plane surface. (On a specular plane surface, 85% of the maximal possible modulation depth results, but only 7.8% results on a rough surface). However, by using the SP-DFT approach, it is still possible to determine reliable distance values. In Fig. 13, surface topographies and horizontal profiles from the middle of the Halle roughness standard 4058/03A1 obtained under different environmental conditions are shown.

First of all, several topographies were obtained without environmental vibrations to compare the roughness parameters with those measured by the manufacturer with a tactile stylus

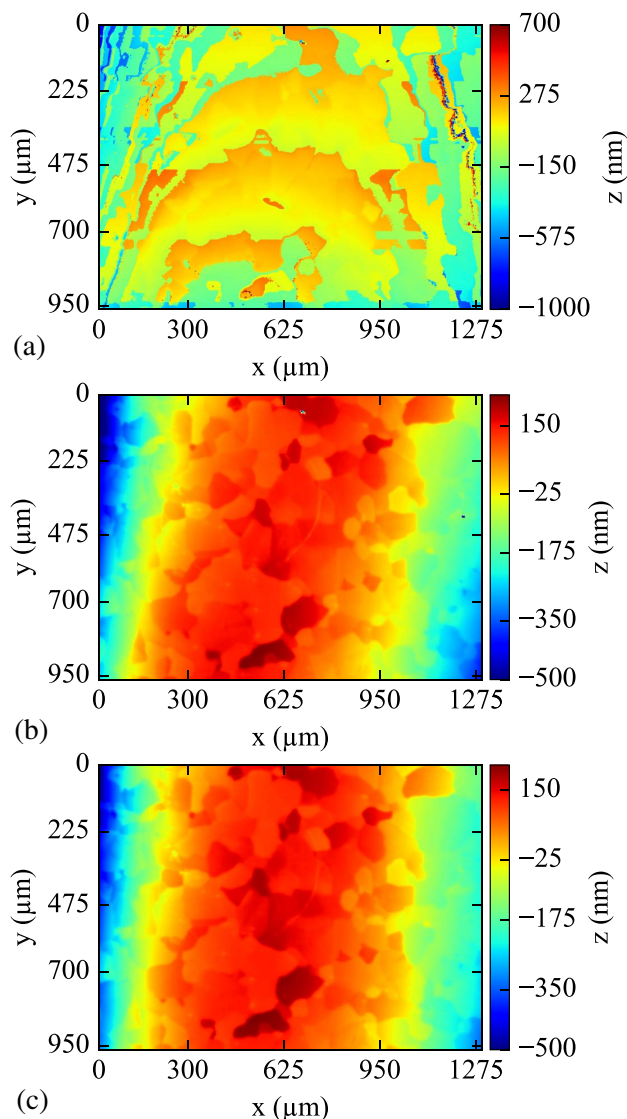


Fig. 12. Topographies of the steel specimen prepared for cyclic fatigue tests. (a) Topography without vibration compensation, (b) topography after vibration compensation, and (c) topography without vibrations obtained in the lab.

instrument. To ensure the comparability of the parameters, several overlapping topography data sets were stitched together to provide the necessary evaluation length. With the presented

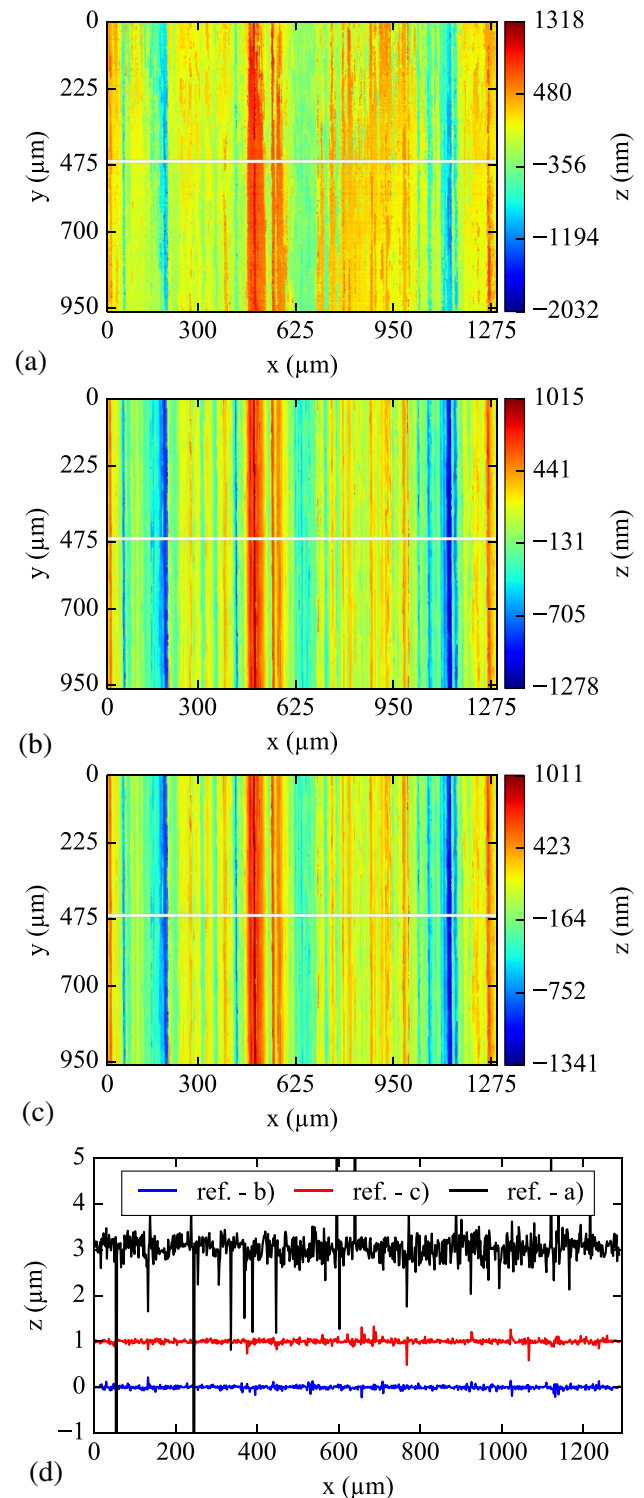


Fig. 13. Topography of the Halle 4058/03A1 roughness standard. (a) Topography from uncorrected, distorted SWLI signals, (b) topography without vibrations, (c) topography after vibration compensation, and (d) height difference between a reference profile and the profiles marked with white horizontal lines in (a)–(c). For better comparability, additional offsets of 1 and $3\text{ }\mu\text{m}$ were added to the red and black curve.

system $R_a = 0.228 \mu\text{m}$ and $R_z = 1.711 \mu\text{m}$ were determined for specimen 4058/03A1. These roughness parameters are within the uncertainty range of $\pm 9\%$ given by the manufacturer and were calculated according to ISO 4287 and ISO 11562 standards. The correction of SWLI signals is also possible in this case, as can be seen from Fig. 13(c). The difference profiles [Fig. 13(d)] illustrate comparable results for the measurements without vibrations (repeatability measurement: blue curve; standard deviation $\sigma_{\text{diff}} = 29.4 \text{ nm}$) and with vibrations but after vibration compensation (red curve; $\sigma_{\text{diff}} = 33.3 \text{ nm}$). The uncorrected profile has a much higher standard deviation of $\sigma_{\text{diff}} = 164 \text{ nm}$ and many spikes in height values resulting from erroneous detection of coherence peak positions in SWLI signals.

Topography measurements on the rougher standard, Halle 4058/03A3, provide similar results. The measured roughness values, $R_a = 1.69 \mu\text{m}$ and $R_z = 8.31 \mu\text{m}$, are within the $\pm 6\%$ uncertainty range given by the manufacturer. Depending on the surface structure under the laser spot of the DMI, the modulation depth of laser interference signal varies between 4% and 18% of maximal possible value. The standard deviation of the difference between two profiles obtained without vibrations is 27.3 nm; with vibrations without correction it is 226 nm, and after correction, 29.3 nm.

As mentioned before, in the second section of this paper, the depth scan is performed by a piezo linear stage (PI N-664) manufactured by Physik Instrumente GmbH (PI). The stage has a closed-loop resolution of 0.5 nm and a linearity of

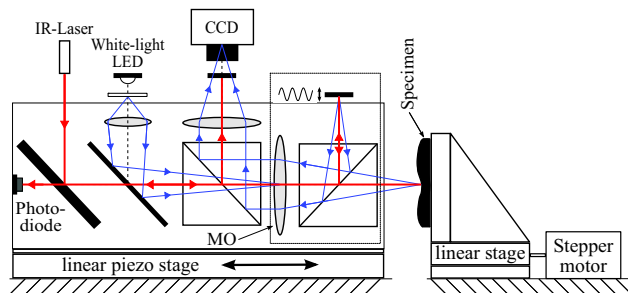


Fig. 14. Sensor with additional scanner axis: the system uses either a piezo linear stage or a stepper motor for the depth scan. The linear stage carrying the specimen is a common manual linear stage equipped with a stepper motor instead of a micrometer screw.

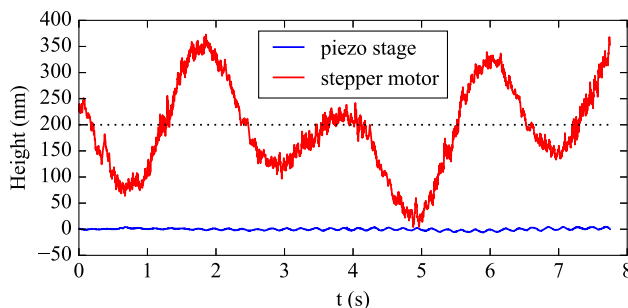


Fig. 15. Deviation from an ideal linear ramp. The maximum deviation for the piezo stage is 6.4 and 196 nm for stepper motor. For better distinguishability between the profiles, an additional offset of 200 nm was added to the stepper motor profile.

5 nm over a range of 20 μm . Consequently, the price of this axis with controller is rather high. With our developed system, we want to demonstrate that it is not necessary to use such expensive scanner axes in white-light interferometry. Instead, we used a stepper motor with a step resolution in the lower micrometer range without any position controlling system to perform a depth scan and to obtain reliable results. Figure 14 shows a schematic sketch of the setup with the additional stepper motor scan axis. A stepper motor with linear transmission

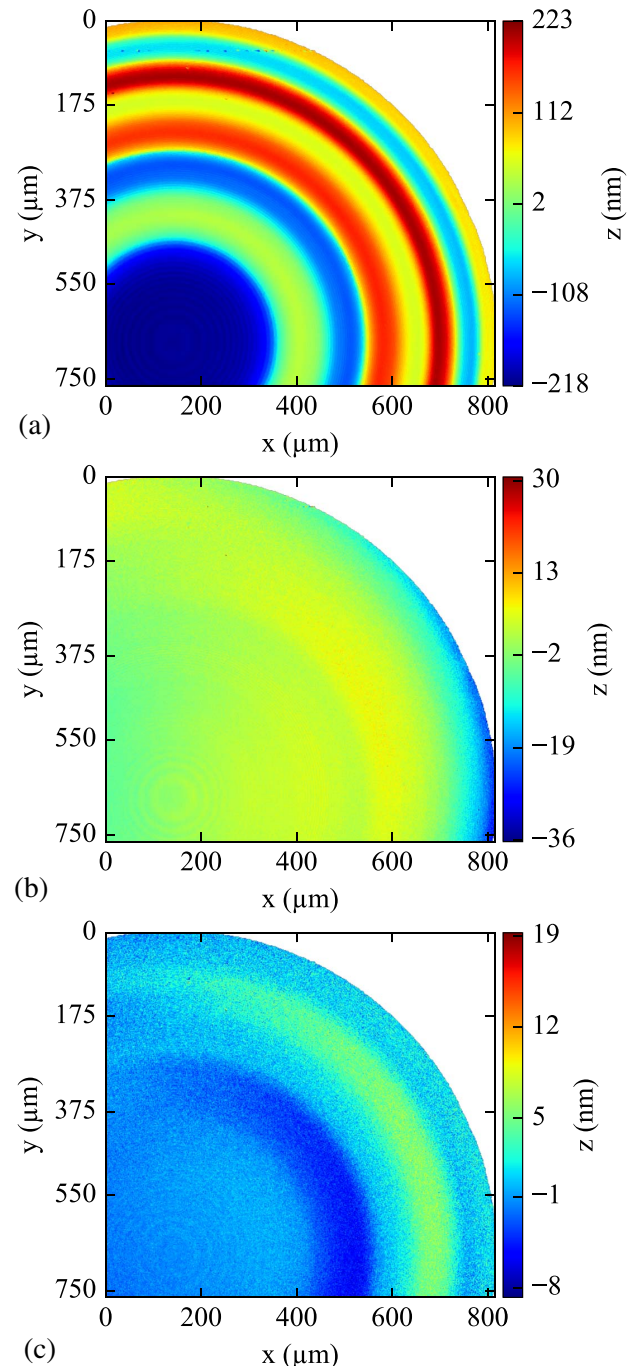


Fig. 16. Residual error maps of a calibration sphere measured with different scanner axes. (a) Stepper motor uncorrected-PI axis, (b) stepper motor corrected-PI axis, and (c) PI axis-PI axis.

replaced the micrometer screw of the manual linear stage. With this setup, we are able to compare both axes with each other by alternating measurements of the same field of view. Figure 15 shows the deviation from linear movement during the depth scan for both axes. As expected, the linearity error of the stepper motor is considerably higher than of the piezo stage. The PI axis has two vibration peaks: at 0.3 Hz with amplitude of 1.2 nm, and at 4.7 Hz with 1.4 nm amplitude. The amplitudes at all other frequencies are below 0.3 nm. The vibrations of the stepper motor are much higher. Two significant peaks appear at 0.3 Hz and 0.5 Hz, with amplitudes of 56 nm and 90 nm, respectively. It also shows a lot of additional peaks in the range of 0–100 Hz with amplitudes ranging from 1 to 4 nm. Usually, nobody would use this axis for high-precision measurements, but by means of the presented compensation method, the axis error can be corrected, and the correct topography can be obtained. The specimen was a calibration sphere (Renishaw) with a diameter of 25 mm. Figure 16 shows the results. A topography data set measured without vibrations using the PI axis is taken as reference and subtracted from the other topographies. In Fig. 16(a), the difference between uncorrected data measured with the stepper motor and the reference topography is shown. The linearity error of the axis results as an additional waviness of the topography. After the correction of the SWLI signals, the topography has noticeably fewer deviations from the reference topography, as can be seen in Fig. 16(b). The standard deviation of the difference is 5.3 nm and is primarily generated by a small lateral misalignment. In the last subfigure [Fig. 16(c)], the difference between the reference topography and another topography obtained under the same conditions is shown. The standard deviation in this case is 2.6 nm.

In the following, we used a Halle groove-depth standard 4080/03 to compare the linearity of both axes. The standard provides six grooves, ranging from 0.24 to 75 μm in depth. For the comparison, grooves of 7.5 and 24 μm depth were used. The groove depths of the specimen are not calibrated by the manufacturer, but they were measured with a commercial confocal microscope (Nanofocus μSurf custom 50 \times , NA = 0.95) to determine their nominal depth. The results are shown in Table 1.

Results in columns titled with “Encoder/Uncorrected” were obtained by using either positions from the internal encoder of the scan axis or assumed steps of the stepper motor. By means of these results, one can see that the linearity error of the stepper

motor is too big for measurements in the nanometer range. However, with signal correction, it is possible to measure the correct depth of the grooves. The results obtained with environmental vibrations were generated by use of the previously mentioned DC motor. The measured disturbance consists mainly of two periodic vibrations at 22 and 89 Hz, with corresponding amplitudes of 100 and 20 nm, respectively. It does not matter whether vibrations during the depth-scan occur or the scanner axis shows positioning errors; the correct surface topography can be reconstructed, and the depths of the grooves can be obtained.

However, this sensor also has its limits. The main restriction is the maximum distance change between two subsequent distance values obtained by the DMI, which should not exceed the ambiguity range of $\pm\lambda/4$. Another limitation is the timestamp of the image acquisition and the timestamp of the nearest distance value. In the actual setup, we use height values from only one flank of the sinusoidal excitation signal, which results in 2 kHz data rate of distance values. Consequently, there is a lag of $\pm 125\ \mu\text{s}$ between the determination of a distance value and the image acquisition by the camera. In case of high vibration amplitude (e.g., 1 μm at approximately 30 Hz) (generated by the already mentioned DC motor driven with higher voltage), the maximal distance change between the image acquisition position and the measured distance value is more than 23 nm. This leads to an erroneous reordering of images under the assumption of a desired spatial sampling interval of 20 nm. The SWLI signal reconstruction fails in this case. This position sampling error can be minimized by using values from both flanks with consecutive interpolation between them. However, the combination of height values from both flanks requires a recalibration of the offset [36]. This calibration should be done without environmental vibrations. Another possibility to reduce the position sampling error is triggering of the LED on the flanks of the mirror movement, but this approach has another drawback. The movement velocity of the reference mirror is maximal at these positions; thus the change in interference contrast is maximal too. This will reduce the contrast of white-light correlograms. Another problem is the LED light pulse, which can be seen in the laser interference signal (cf. Fig. 3 at 0.7 ms). Although a cold-light reflector is used, it does not completely block the white light; the remaining intensity is enough to generate a significant peak in the laser interference signal. By an overall low modulation depth

Table 1. Comparison of Measured Groove Depths with Piezo Linear Stage (PI) and Stepper Motor without and with Environmental Vibrations^a

Nominal Depth		7525 nm			
Scan Axis	Without Vibrations		With Vibrations		
	Encoder/Uncorrected	DMI-Based Correction	Encoder/Uncorrected	DMI-based Correction	
PI	7526.0 \pm 2.8	7521.4 \pm 0.5	7881.4 \pm 495.3	7522.1 \pm 0.4	
Stepper motor	8099.8 \pm 4.8	7521.3 \pm 0.3	7604.6 \pm 218.6	7522.0 \pm 0.2	
Nominal depth		24003 nm			
PI	23994.2 \pm 4.0	23993.1 \pm 0.6	23553.8 \pm 635.5	23995.9 \pm 2.1	
Stepper motor	24529.8 \pm 19.0	23991.6 \pm 0.1	24229.6 \pm 113.0	23993.2 \pm 0.6	

^aAll values are in nanometer units. Each measurement was repeated three times.

(e.g., measurement on a rough surface) such a peak would lead to erroneous signal evaluation and could result in a phase jump in the distance course.

5. CONCLUSION AND OUTLOOK

A passive vibration compensation technique in SWLI was described, which is well suited for measurements even under difficult environmental conditions. During the white-light depth scan, an integrated DMI measures distance changes with high temporal and distance resolution. The measured distance changes are used to correct white-light interference signals subsequent to the measurement. The surface topography is then obtained by using common signal evaluation algorithms. Measurements on different objects in the presence of mechanical vibrations demonstrate the capabilities of the presented system.

Currently, only a single laser spot is used to measure distance changes. Depending on the surface topography, it is possible that some areas are less reflective or nonreflective. Thus, the distance measurement can fail. In future, we intend to use several laser spots spread over the field of view to measure distance changes at different positions. This will not only further increase the robustness of the distance measurements, but it will also provide a possibility to measure tilt/tip of the surface caused by vibrations.

Improved wavelength separation in combination with even shorter light pulses would allow the triggering of the LED on rising or falling flanks of the mirror deflection and would decrease the deviation between the trigger position and distance measurement. In addition, increasing the frequency of the excitation signal is another option to get rid of this problem.

DMI integration in other types of interferometers, such as Linnik or especially Mirau, would extend possible applications of this vibration compensation technique.

Funding. Deutsche Forschungsgemeinschaft (DFG) (LE 992/9-1).

REFERENCES

1. B. C. Lee and T. C. Strand, "Profilometry with a coherence scanning microscope," *Appl. Opt.* **29**, 3784–3788 (1990).
2. L. Deck and P. de Groot, "High-speed noncontact profiler based on scanning white-light interferometry," *Appl. Opt.* **33**, 7334–7338 (1994).
3. P. de Groot and L. Deck, "Surface profiling by analysis of white-light interferograms in the spatial frequency domain," *J. Mod. Opt.* **42**, 389–401 (1995).
4. A. Harasaki, J. Schmidt, and J. C. Wyant, "Improved vertical-scanning interferometry," *Appl. Opt.* **39**, 2107–2115 (2000).
5. M. Fleischer, R. Windecker, and H. J. Tiziani, "Fast algorithms for data reduction in modern optical three-dimensional profile measurement systems with MMX technology," *Appl. Opt.* **39**, 1290–1297 (2000).
6. T. Gruebler and P. Drabarek, "Interferometric measuring system for cone inspection on shop-floor level," *Proc. SPIE* **9525**, 95250O (2015).
7. H. Martin, K. Wang, and X. Jiang, "Vibration compensating beam scanning interferometer for surface measurement," *Appl. Opt.* **47**, 888–893 (2008).
8. X. Jiang, K. Wang, F. Gao, and H. Muhamedsalih, "Fast surface measurement using wavelength scanning interferometry with compensation of environmental noise," *Appl. Opt.* **49**, 2903–2909 (2010).
9. H. Muhamedsalih, X. Jiang, and F. Gao, "Vibration compensation of wavelength scanning interferometer for in-process surface inspection," in *Future Technologies in Computing and Engineering: Proceedings of Computing and Engineering Annual Researchers Conference (CEARC)*, (University of Huddersfield, 2010), pp. 148–153.
10. P. Schaefer, D. Broschart, and J. Seewig, "Aktive Schwingungsdämpfung eines Weißlichtinterferometers," *Tech. Mess.* **80**, 16–20 (2013).
11. G. C. Cole, J. H. Burge, and L. R. Dettmann, "Vibration stabilization of a phase shifting interferometer for large optics," *Proc. SPIE* **3134**, 438–446 (1997).
12. C. Zhao and J. H. Burge, "Vibration-compensated interferometer for measuring cryogenic mirrors," *Proc. SPIE* **3782**, 399–406 (1999).
13. L. L. Deck, "Suppressing phase errors from vibration in phase-shifting interferometry," *Appl. Opt.* **48**, 3948–3960 (2009).
14. J. Park and S. Kim, "Vibration-desensitized interferometer by continuous phase shifting with high-speed fringe capturing," *Opt. Lett.* **35**, 19–21 (2010).
15. A. Olszak and J. Schmit, "High-stability white-light interferometry with reference signal for real-time correction of scanning errors," *Opt. Eng.* **42**, 54–59 (2003).
16. J. Schmit, A. Olszak, and S. McDermed, "White light interferometry with reference signal," *Proc. SPIE* **4777**, 102–109 (2002).
17. D. Chen, J. Schmit, and M. Novak, "Real-time scanner error correction in white light interferometry," *Proc. SPIE* **9276**, 92760I (2014).
18. H. Broistedt, N. R. Doloca, S. Strube, and R. Tutsch, "Random-phase-shift Fizeau interferometer," *Appl. Opt.* **50**, 6564–6575 (2011).
19. R. Smythe and R. Moore, "Instantaneous phase measuring interferometry," *Opt. Eng.* **23**, 361–364 (1984).
20. J. Millerd, N. Brock, J. Hayes, M. North-Morris, M. Novak, and J. Wyant, "Pixelated phase-mask dynamic interferometer," *Proc. SPIE* **5531**, 304–314 (2004).
21. J. T. Wiersma and J. C. Wyant, "Vibration insensitive extended range interference microscopy," *Appl. Opt.* **52**, 5957–5961 (2013).
22. E. Cucho, F. Bevilacqua, and C. Depeursinge, "Digital holography for quantitative phase-contrast imaging," *Opt. Lett.* **24**, 291–293 (1999).
23. J. Kühn, T. Colomb, F. Montfort, F. Charriere, Y. Emery, E. Cucho, P. Marquet, and C. Depeursinge, "Real-time dual-wavelength digital holographic microscopy with a single hologram acquisition," *Opt. Express* **15**, 7231–7242 (2007).
24. O. Sasaki and H. Okazaki, "Sinusoidal phase modulating interferometry for surface profile measurement," *Appl. Opt.* **25**, 3137–3140 (1986).
25. M. Schulz and P. Lehmann, "Measurement of distance changes using a fibre-coupled common-path interferometer with mechanical path length modulation," *Meas. Sci. Technol.* **24**, 065202 (2013).
26. H. Knell, S. Laubach, G. Ehret, and P. Lehmann, "Continuous measurement of optical surfaces using a line-scan interferometer with sinusoidal path length modulation," *Opt. Express* **22**, 29787–29797 (2014).
27. J. Schmit, "High speed measurements using optical profiler," *Proc. SPIE* **5144**, 46–56 (2003).
28. S. Tereschenko, P. Kühnhold, P. Lehmann, L. Zellmer, and A. Brückner-Foit, "Tiefenscannende Weißlichtinterferometrie in maschinennaher Umgebung," *Tech. Mess.* **81**, 269–279 (2014).
29. P. de Groot, "Design of error-compensating algorithms for sinusoidal phase shifting interferometry," *Appl. Opt.* **48**, 6788–6796 (2009).
30. P. Hariharan, B. F. Oreb, and T. Eiju, "Digital phase-shifting interferometry: a simple error-compensating phase calculation algorithm," *Appl. Opt.* **26**, 2504–2506 (1987).
31. K. Creath, "Phase-measurement interferometry techniques," in *Progress in Optics*, E. Wolf, ed. (Elsevier, 1988), Vol. **26**, Chap. V, pp. 349–393.
32. S. Tereschenko, P. Lehmann, P. Gollor, and P. Kühnhold, "Robust vertical scanning white-light interferometry in close-to-machine applications," *Proc. SPIE* **9525**, 95250Q (2015).
33. L. Reichel, G. S. Ammar, and W. B. Gragg, "Discrete least squares application by trigonometric polynomials," *Math. Comput.* **57**, 273–289 (1991).
34. J. Liesener, M. Davidson, P. de Groot, X. C. de Lega, and L. Deck, "Low coherence interferometry with scan error correction," U.S. patent 8,902,431 B2 (Dec 2, 2014).
35. M. R. Craymer, "The least squares spectrum, its inverse transform and autocorrelation function: theory and some applications in geodesy," Ph.D. dissertation, Doctor of Philosophy, Graduate Department of Civil Engineering, (University of Toronto, 1998).
36. M. Schulz, T. Wagner, and P. Lehmann, "Fiber-coupled interferometric sensor for high-speed measurement of optical surfaces," in *Optical Measurement Techniques for Systems and Structures III*, J. J. Dirckx, ed. (Shaker, 2016), pp. 277–288.